
Continuum versus discrete flux behaviour in large mesoscopic $\text{Bi}_2\text{Sr}_2\text{CaCu}_2\text{O}_{8+\delta}$ disks

M. R. CONNOLLY¹, M. V. MILOŠEVIĆ^{1,2}, S. J. BENDING¹, JOHN R. CLEM³ and T. TAMEGAI⁴

¹ *Department of Physics, University of Bath, Claverton Down, Bath, BA2 7AY, UK.*

² *Departement Fysica, Universiteit Antwerpen, Groenenborgerlaan 171, B-2020 Antwerpen, Belgium.*

³ *Ames Laboratory, Department of Physics and Astronomy, Iowa State University, Ames, IA 50011-3160, USA.*

⁴ *Department of Applied Physics, The University of Tokyo, Hongo, Bunkyo-ku, Tokyo 113-8656, Japan.*

PACS 74.78.-w – Superconducting films and low-dimensional structures
PACS 74.25.Ha – Magnetic properties
PACS 74.72.Hs – Bi-based cuprates

Abstract. - Scanning Hall probe and local Hall magnetometry measurements have been used to investigate flux distributions in large mesoscopic superconducting disks with sizes that lie near the crossover between the bulk and mesoscopic vortex regimes. Results obtained by directly mapping the magnetic induction profiles of the disks at different applied fields can be quite successfully fitted to analytic models which assume a continuous distribution of flux in the sample. At low fields, however, we do observe clear signatures of the underlying discrete vortex structure and can resolve the characteristic mesoscopic compression of vortex clusters in increasing magnetic fields. Even at higher fields, where single vortex resolution is lost, we are still able to track configurational changes in the vortex patterns, since competing vortex orders impose unmistakable signatures on “local” magnetisation curves as a function of the applied field. Our observations are in excellent agreement with molecular dynamics numerical simulations which lead us to a natural definition of the lengthscale for the crossover between discrete and continuum behaviours in our system.

Developing computational techniques that can span multiple length-scales is a major focus of research in modern day nanotechnology. Models of nanoscale transistors must, for example, be able to describe them from the microscopic level of discrete electron dynamics all the way up to the macroscopic scale of contact pads, bond wires and packaging. An attractive feature of using so-called multiscale methods is that the physics of the discrete components is embedded in parameters used at the coarse scale without dramatically increasing the analytical and computational overhead. A certain degree of added complexity is often unavoidable when using such methods, however, especially when the fine scale properties are included without using approximations, and as a result most physical problems are in reality still described at either the discrete or continuum level. The application of continuum models to systems composed of discrete components is a core concept common to all of the natural sciences. In physics, for example, the semi-classical conductivity tensor is a continuum approximation of the discrete quantum-mechanical

Landauer-Buttiker formalism, which views conductance as the transmission of individual electrons. Continuum elasticity has been hugely successful in describing many of the properties of structural materials, yet plastic deformation can only be understood by considering the discrete nature of solids and the atomic-scale dislocation dynamics. Since the two approaches are nearly always exclusive the key to successful multiscale modelling is establishing where the crossover lengthscale between discrete and continuum behaviours actually lies, and finding theoretical descriptions capable of bridging it.

Vortex matter in superconductors represents an ideal model system for studying the continuum/discrete crossover, since the vortex density and interaction strengths can be continuously tuned by varying the magnetic field. One of the key topological properties of a type II superconductor in an applied magnetic field is the penetration and collective triangular ordering of mutually repelling lines of magnetic flux (i.e. vortices), into the so-called Abrikosov lattice. If, however, the size of

a superconducting sample is reduced to mesoscopic dimensions, it is well known that the interaction between the penetrating vortices and the circulating edge currents can become comparable to the intervortex repulsion, leading to the destruction of the ordered triangular lattice. Deep in the mesoscopic regime, where the sample size is comparable to the penetration depth λ and/or the coherence length ξ , this “topological confinement” is so strong that the sample geometry imposes its symmetry on multi-vortex states [1]. In superconducting disks this results in the arrangement of vortices in concentric shells [2] or their collapse into a single multi-quantum vortex [3]. The behaviour of vortex matter when the size of a sample is between the mesoscopic, where the position of each vortex has a direct influence on its superconducting state, and the macroscopic, where the only relevant parameter is the “local” vortex density, remains an open question. In this “large mesoscopic” regime, superconductivity coexists with a large number of vortices, which may or may not be organized into an Abrikosov lattice (see Ref. [4], or [5] for the analogy with confined classical clusters.) To date only a few studies have been able to access this regime experimentally [6, 7]. Available imaging techniques have proved to be unable to resolve individual vortices at large applied fields, while “local” magnetisation curves do not generally exhibit discontinuities that can be directly associated with the transitions between different fluxoid states seen in smaller mesoscopic disks [8]. In the absence of strong features related to individual vortices, the quasi-continuous magnetisation curves and flux profiles of large superconducting disks can be rather well described by classical continuum electromagnetism [9, 10]. The primary objective of this Letter is to address how the discrete and continuum descriptions can be used almost interchangeably to describe the superconducting state of disks with dimensions near this meso-to-macro crossover point. We have explored this regime both experimentally, using scanning Hall probe microscopy (SHPM) [11] and “local” magnetometry of high- T_c superconducting disks, and theoretically using modified molecular dynamics numerical simulations. We have fabricated periodic arrays of large mesoscopic disks on the surface of an optimally doped $\text{Bi}_2\text{Sr}_2\text{CaCu}_2\text{O}_{8+\delta}$ (BSCCO) single crystal ($T_c \approx 91$ K). Single crystal high- T_c materials are excellent candidates for studies in the large mesoscopic regime due to their low pinning, readily accessible temperatures of interest, and large λ/ξ ratio (known as the Ginzburg-Landau parameter κ), all of which combine to ensure that vortices are able to attain the highly ordered ground state shell structures.

The disks were patterned to a depth of $d = 300$ nm into the surface of a BSCCO crystal of dimensions ≈ 2 mm \times 2 mm \times 100 μm using photolithography and Ar-ion beam milling. The array consisted of 5 μm , 10 μm , 15 μm and 20 μm diameter disks sited on the corners of a square cell with 20 μm sides inclined at 45° to the crystallographic a -axis of the crystal (a typical region is shown

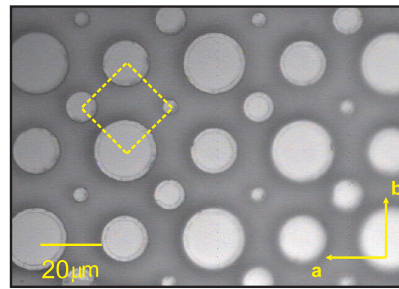


Fig. 1: Optical micrograph of the disk array showing the orientation of the 20 μm \times 20 μm square cell (dashed lines) and the directions of the crystallographic a - and b -axis of the BSCCO crystal.

in Fig. 1). The patterned area of the crystal (typically 1-2 mm²) was bonded to a Si substrate for mechanical stability. The sample was coated with Ti(5 nm)/Au(20 nm) films to enhance the stability of the SHPM when in tunnelling contact. In our first experiments the array was cooled to $T = 77$ K and SHPM images were captured at regular (increasing) field intervals. Fig. 2(a) illustrates how we subtract the pixels ($B_{i,j}^d = B_{i,j}^2 - B_{i,j}^1$) of two SHPM scans captured in different magnetic fields to construct “difference” images. These are used in this study to enhance the contrast due to small numbers of penetrating vortices which cannot be resolved in raw SHPM images. As expected [9, 10], for fields just above the penetration field H_p , a central vortex “dome” is formed which expands with increasing applied field in both the 20 μm and 10 μm diameter disks [see insets in Fig. 2(b)]. While the “local” edge field at which the dome forms must be almost the same in both disks, the greater enhancement of the applied field around the 20 μm disks (i.e. the larger demagnetisation factor) leads to a reduction of the measured penetration field. Figure 2(b) shows plots of the radius, b , of the dome of penetrated flux as a function of the applied field, H_z , for the two disk sizes. To obtain $b(H_z)$, difference images at a given applied field were constructed with respect to a vortex-free reference state just below penetration ($H_p \approx 6.25$ Oe and 4.5 Oe for the 10 μm and 20 μm disks respectively). Linescans from the central peak of the dome to the minimum at its perimeter were taken along different radial directions to find an average value for the dome radius. The experimental form of $b(H_z)$ illustrates how the dome expands rapidly within a few Oersteds of the penetration field and then saturates upon approaching the high-density screening currents close to the disk edge.

Although the disks in our system are actually sitting on top of a BSCCO platelet we argue that this plays no role since bulk vortex pinning will be negligibly small at our measurement temperature. Focussing first on the 20 μm disk, our observations find a natural explanation within continuum models for flux penetration [9, 10] in which vortices nucleate when the applied field reaches the minimum field required for thermal activation of pancake vortices

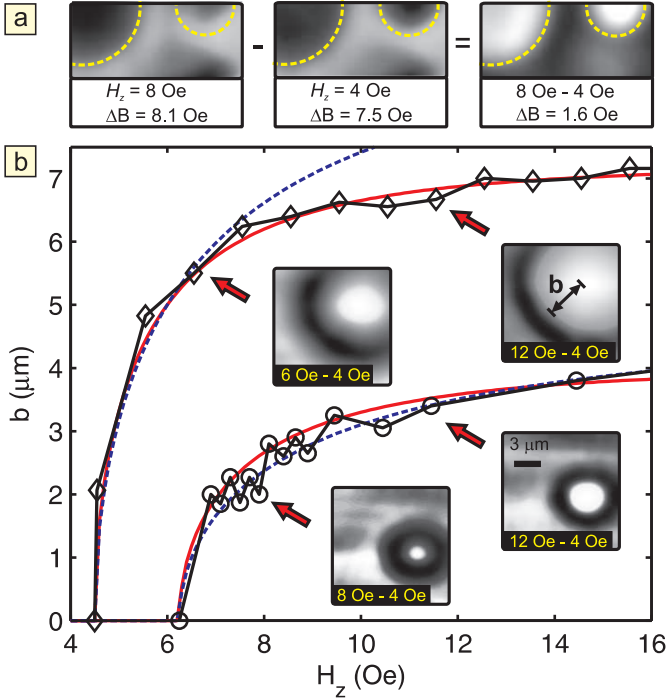


Fig. 2: (a) $10 \mu\text{m} \times 26 \mu\text{m}$ SHPM images captured in two applied fields at $T = 77$ K and their difference image. Dashed outlines indicate the location of two of the disks. (b) Radius b of the vortex dome versus the applied field, H_z , for the $10 \mu\text{m}$ (o) and $20 \mu\text{m}$ (\diamond) diameter disks. Insets show typical difference images used to extract the experimental points. The solid lines are fits to the measured data using a continuum model [9] and the dashed lines denote the relation for the instability radius of vortex molecules from Ref. [4].

over the Bean-Livingston surface barrier (BLb). Note that in the absence of the BLb and demagnetisation effects this field would simply be H_{c1} . In terms of the radially distributed current density, $J(r)$, the entrance condition is equivalent to requiring a critical current density at the sample edge. Analytic expressions for $J(r)$ follow from the approximation that the current density is zero within the vortex dome ($r < b$) and the magnetic induction is zero in the vortex-free region ($b < r < R$) [9]. The application of the analytical results of the strip model to our disks is justified by a number of studies, particularly the numerical simulations of pin-free samples conducted in Ref. [12], where the magnetisation in the two geometries shows qualitatively identical behaviour if the strip is chosen to be twice as thick as the disk. At a given value of H_z , a steady state is reached when the radius of the dome satisfies $b = R' \sqrt{1 - (H_p/H_a)^2}$ and the solid lines in Fig. 2(b) represent fits to this expression using R' as a fitting parameter (in the case of a strip, R' is equal to the half-width). The agreement between theory and experiment is good (we find $R' = 7.16 \mu\text{m}$ for the upper curve, and $3.5 \mu\text{m}$ for the lower curve of Fig. 2(b), close to the expected 2:1 ratio), and to our knowledge this result is the first direct experimental validation of the assumptions behind

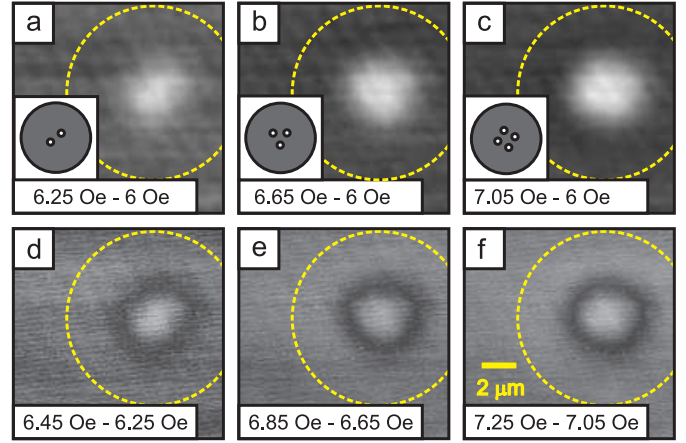


Fig. 3: (a)-(c) Sequence of SHPM difference images showing the evolution of vortex clusters (white) with 2, 3, and 4 vortices in a $10 \mu\text{m}$ disk. Insets show sketches of the proposed vortex configurations. (d)-(f) “Difference” images between states with the same vorticity in different applied fields, corresponding to the vorticity for (a)-(c) respectively.

continuum models for the field-dependence of the vortex dome. We note that an alternative form for the critical entry condition was derived specifically for thin disks by Babaei Brojeny and Clem [13], but was found to rise more abruptly than the experimentally found H_p .

In contrast, it is quite apparent from Fig. 2(b) that the continuum expression fails to describe the oscillatory behaviour of $b(H_z)$ observed at low fields in the $10 \mu\text{m}$ disk. The origin of these features can be seen in the SHPM images of vortex clusters with 2, 3, and 4 vortices shown in Fig. 3(a)-(c). Although the shape of the cluster in each case allows us to determine the number of vortices without ambiguity, the strong overlap of the vortex fields hampers the resolution of their exact core positions. The field increment was reduced to just below the field step, ΔH_1 , required to nucleate an additional vortex in the $10 \mu\text{m}$ disk ($\Delta H_1 = \Phi_0/\pi R^2 \approx 0.263$ Oe) and the images in Fig. 3(d)-(f) show “difference” images between states with the same vorticity in two different applied fields. The dark “rings” correspond to a reduction in the local flux density where the vortices have moved closer to the centre and represent the first direct evidence for the compression of vortex clusters in increasing applied fields. This is a distinctive mesoscopic effect, caused by the interaction between vortices and the increasing Meissner currents at the disk edge. Considering that the edge currents decay away from the boundary on the scale of the penetration depth ($\lambda \approx 400$ nm in our sample,) this striking observation of the “breathing” mode of vortex configurations is surprising given the large size of the disk ($R > 12\lambda$) and clearly supports the classification for this disk as “large mesoscopic”. Returning now to the discussion of Fig. 2(b), a suitable expression for $b(H_z)$ accounting for the discrete composition of the dome has been derived in the limit of large κ ,

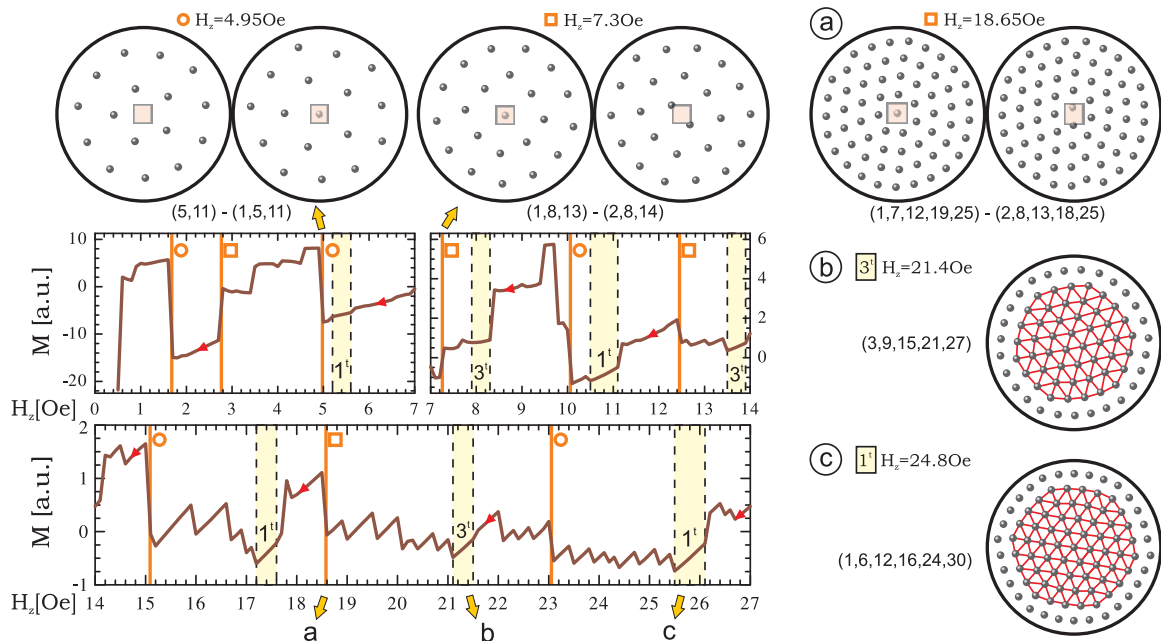


Fig. 4: The calculated magnetisation in decreasing applied magnetic field. The circular snapshots show characteristic vortex configurations [for a complete data set, see the animations in the supplementary material] and illustrate the origin of the features in the $M(H_z)$ curve measured across the depicted Hall probe (shaded square). In the main panel, open circles indicate a collapse of a shell, while open squares denote the reduction of the innermost shell to a single vortex.

$\Lambda = \lambda^2/d > R$, and $d \ll \lambda$ in Ref. [4]. By considering the forces on vortices arranged in a regular polygon encircled by a ring of radius, b , Cabral et al. [4] obtained $b(H_z)$ at which each vortex cluster becomes unstable with respect to the entrance of the next vortex. This radius is clearly the discrete counterpart of the dome radius, b , in the continuum limit, and is given by $b = R'' \sqrt{1 - (\Delta H_1/H_a)}$. As it stands, however, this expression cannot be compared to the measured data because it states, unrealistically, that penetration occurs simply when the net flux over the area of the disk is a single flux quantum, thus ignoring the screening effects. Since the magnitude of magnetic screening cannot be estimated with great precision, we assume instead that the qualitative form is correct and simply set the offset field, ΔH_1 , equal to the penetration field H_p , and fit the above expression to the data for both disks, again using R'' as a free parameter. The best fits are shown as dashed curves in Fig. 2(b), and were obtained for R'' equal to $5.1 \mu\text{m}$ and $8.9 \mu\text{m}$ for the $10 \mu\text{m}$ and $20 \mu\text{m}$ diameter disks, respectively. The qualitative fit to the data is good for the $10 \mu\text{m}$ disk (and $R \approx R''$) but evidently fails for the $20 \mu\text{m}$ disk, strongly suggesting that the crossover from discrete to continuum behaviour occurs between these two disk sizes.

In the light of these observations we attempt to describe the discrete properties of our system theoretically using a modified molecular dynamics approach based on London theory, which shows excellent correspondence to the more complex Ginzburg-Landau formalism in the extreme type-II limit. Ref. [4] outlines the derivation of the vortex-

vortex and vortex-boundary interaction potentials from the expression for the free energy of small superconducting disks. However, samples of intermediate size, i.e. with $d \sim \lambda$ and $R > \lambda, \Lambda$ have not been described in any simplifying limit up to date. Nevertheless, although our samples are significantly larger than λ , the results shown in Fig. 3 suggest a very strong influence of the boundary on the vortex configurations. On the basis of this empirical evidence we use the mesoscopic approximation for $10 \mu\text{m}$ diameter disks, and exploit Eqs. (12-14) from Ref. [4] to perform the presented simulations. For the viscous drag coefficient, η , we take the field-dependent Bardeen-Stephen expression [14]. A key feature of our model is the investigation of configurational changes in the vortex states in decreasing field. Starting from high applied field and a large number (≈ 100) of vortices, we track states with same vorticity as long as they are stable. In decreasing field, the previously found state is used as an initial configuration for the next, and we allow vortices at the boundary to leave the sample as the Bean-Livingston barrier decreases. This model closely corresponds to the experimental situation in which an applied magnetic field is swept down, since the weakening of the screening currents close to the vortex expulsion field favours the applicability of the London approximation (in general, London theory neglects the suppression of superconductivity on the disk edges due to circulating Meissner currents). For sequential vortex states in decreasing field, the magnetisation of the sample was calculated by integrating all (Pearl) vortex fields [15]. To link the approach to the current experiments even more closely,

we perform the integration at a scanning height of $z = 300$ nm through a $1 \times 1 \mu\text{m}^2$ square area above the centre of the disk (a situation which corresponds to a realistic Hall probe). The magnetic response, starting from a maximum vorticity of 100, is shown as a function of applied field in Fig. 4. As anticipated, each change in vorticity is accompanied by a jump in the magnetisation curve. However, in addition to these features we also observe a series of significantly larger jumps, which stem directly from the reconfiguration of vortices in the sample¹.

It is already well known that vortices in mesoscopic disks tend to form shell structures [2]. Although the evolution of the number of vortices occupying each shell strongly depends on the size of the disk and the applied field, in decreasing fields it is always the case that the innermost shell collapses first. Prior to this the number of vortices in the centre of the disk gradually decreases, and the final collapse of the shell is marked by the integration of the last central vortex into the other shells (for illustration, see configurations (1, 5, 11) \rightarrow (5, 11) in Fig. 4). For a Hall probe placed above the centre of the disk, there is consequently always a sharp increase in the measured magnetisation when a shell collapses, as is indicated by open circles in Fig. 4 (the first such transition is at 23.1 Oe). In agreement with studies of colloidal systems [16], we never observe more than 5 vortices in the new innermost shell. Further decrease of the applied field relieves the magnetic pressure at the centre, and the number of vortices in the central cluster decreases. The effect of the transitions between multi-vortex structures is subtle because it depends on the size of the cluster compared to the size of the Hall probe. In principle, the reduction of the vorticity under the probe increases the measured magnetisation (see for instance the transition at 18.65 Oe and the corresponding configurations in Fig. 4). However, for low vortex densities the cluster size may exceed the size of the probe. With all vortices in a cluster being effectively around the probe, the measured magnetisation now decreases when the vorticity is lowered (see transitions marked by an open square for fields below 10 Oe, and inset configurations for $H_z = 7.3$ Oe in Fig. 4).

In addition to the discontinuities in the magnetisation that are due to reconfiguration, we have also identified several vortex states of pronounced stability, shown by dashed lines in Fig. 4. All of these states show a triangular arrangement of vortices (with either one (1^t) or three (3^t) vortices in the disk centre) which gradually deforms to a shell structure near the disk boundary. *In actual fact, the latter structures are simultaneously triangular and shell-like, and therefore clearly minimise the energy of a large mesoscopic disk by combining the energetically favourable vortex arrangements seen in the bulk and mesoscopic limits.* This absolute minimisation of intervortex interactions results in a stable locking of the vorticity over a finite

¹An animated sequence of all vortex configurations corresponding to Fig. 4 is available at <http://www.ua.ac.be/milorad.milosevic>.

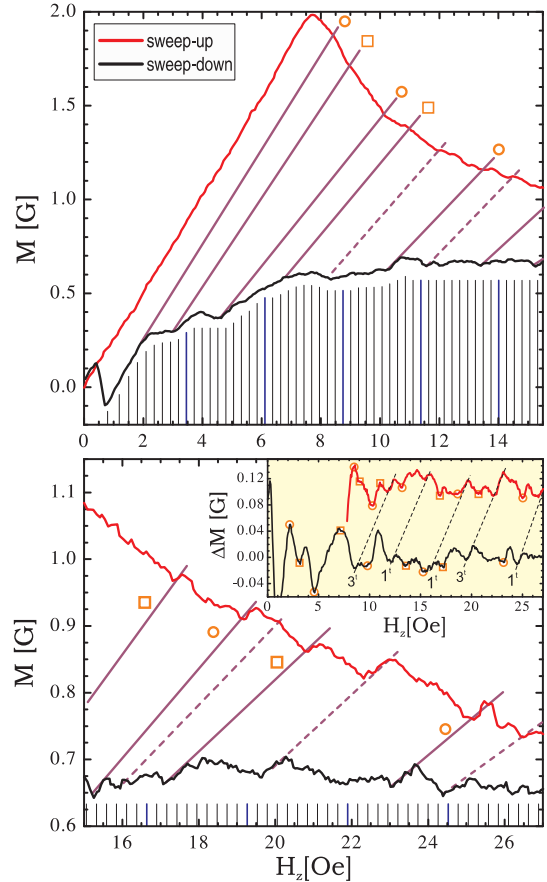


Fig. 5: Experimentally obtained “local” $M(H_z)$ curves, for increasing (red) and decreasing (black) fields. Slanted lines indicate vortex transitions of the same kind in sweep-up and sweep-down traces; connected points on both curves are clearly marked in the inset, where the background variation of $M(H_z)$ has been subtracted to extract the discontinuities arising from configurational changes. Vertical lines show the expected ground state transition fields between states with sequential vorticities [2], where the blue lines indicate the fields at which the vorticity is a multiple of ten to facilitate the counting.

range of applied fields, as observed in Fig. 4.

In Fig. 5 we present the experimentally measured “local” magnetisation ($M = B_z - \mu_0 H_z$) captured with the SHPM Hall sensor parked at the centre of a $10 \mu\text{m}$ disk. The applied field, H_z , was swept around a measurement cycle between ± 36 Oe and the local magnetic induction at the Hall sensor, B_z , was recorded at each point. The first “virgin” trace was discarded, and the subsequent 50 cycles then averaged to improve the signal-to-noise ratio still further. The top curve in Fig. 5 was obtained in increasing field and is different to the curve measured in decreasing field due to hysteretic flux entry/exit. Nevertheless, by following the pattern of magnetic signatures shown in Fig. 4, we were able to identify and link pronounced features in sweep-up and sweep-down curves, as labelled by the slanted lines in Fig. 5. Remarkably, almost all magnetisation jumps predicted by the numerical

simulation were indeed found in the experimental data at virtually the same values of the applied field on the sweep-down leg of the curve. The solid slanted lines in Fig. 5 therefore represent transitions of the same type: either a new shell formation or a single- to multi-vortex transition in the innermost shell. We emphasise that while the vortex configurations at which these transitions occur are not necessarily the same in increasing and decreasing fields, the states with the same vorticity in the combined shell-triangular structure, which are linked by the dashed lines, do appear in both sweep directions due to their enhanced topological stability. Regardless of their exact origin, it is clear that the slopes of the transition lines drawn in Fig. 5 gradually decrease with increasing field. At larger fields, and consequently larger vorticity, the screening currents are strongly compensated by the vortex currents, and the lines gradually deviate from the Meissner slope observed prior to flux penetration. For the sake of completeness we also show the expected vorticity in the ground-state as a function of applied field in Fig. 5, using the expression from Ref. [2].

Finally, we use this competition between the triangular ordering of a lattice and deformation into vortex shells to define a criterion for the meso- to macroscopic crossover. For high vortex densities, a perfect triangular lattice would be ideally fitted into a superconducting disk in such a way that apices of its hexagonal footprint sit at a distance λ from the disk boundary. Vortices along the straight edges of the outer hexagon experience a net outward force which makes the formation of a shell more favourable and diminishes with increasing size of the disk. Balancing all the forces acting on the central vortex on one edge of this outer hexagon, we obtain an equality

$$\frac{R - \Lambda}{a} \sqrt{3} f_{vv}(r, r - \frac{a}{R}) + \frac{r}{1 - r^2} = rL \frac{2.491 + 0.617L}{0.402 + 0.598L}, \quad (1)$$

where a is the lattice constant of the triangular lattice, $r = (1 - \Lambda/R)\sqrt{3}/2$ is the location of the test vortex (scaled to R), $f_{vv}(x_1, x_2) = 1/(x_1 - x_2) - x_2^2/(x_2^2 x_1 - x_2)$ is the dimensionless vortex-vortex interaction, and $L = 3n(n + 1) + 1$ is the total number of vortices in a perfect triangular lattice with n hexagonal shells around the central vortex. The first term in Eq. (1) sums up the interactions of the test vortex with all others (with position r_i), using the empirically determined fact that $\sum_{r-r_i \leq a} f_{vv}(r, r_i) \approx \sum_{ka < r-r_i \leq (k+1)a} f_{vv}(r, r_i)$, for $k = 1, 2, \dots$ (f_{vv} decays as $1/\rho$ at distance ρ from the test vortex, but the number of vortices in the surrounding shells grows proportional to ρ). Second term in Eq. (1) describes the interaction of the test vortex with the boundary, while the right side of the equation gives the interaction with the shielding currents, induced by the field $h = \frac{b+cL}{e+fL} \frac{\Phi_0}{\pi R^2}$ which stabilizes a state with vorticity L as an energy minimum (c.f. Ref. [2] for exact coefficients). Taking $a = \Lambda \approx 533$ nm to be the limiting case for “magnetically” distinguishing between vortices in the lattice, and number of shells $n = 8$,

Eq. (1) yields $R \approx 9.91\Lambda = 5.28 \mu\text{m}$ (and grows further with n), which falls within the crossover regime where our experiments are performed.

In conclusion, we have presented the first experimental study of large mesoscopic superconductors (high- T_c disks) which has been able to demonstrate both macro- and mesoscopic behaviour. In disks of $20 \mu\text{m}$ diameter, we have imaged the growth of the flux dome and successfully fitted its observed expansion using analytic continuum models. The latter models failed however to describe flux penetration in $10 \mu\text{m}$ disks, in which we were able to directly image the compression of small vortex clusters in increasing fields. Even at higher fields where the continuum model regains validity, the system continues to exhibit discreteness through characteristic features in the “local” $M(H_z)$ curves. These measurements, in combination with numerical simulations, allow us to identify the magnetic signatures of individual vortices penetrating the centre of the disk, the assembly process of vortices into different shell formations, and the collective locking of flux lines into configurations which are simultaneously triangular and concentric. Finally, the competing effects between Abrikosov lattice and shell-like ordering have allowed us to develop an analytic criterion which places the “large mesoscopic” regime for superconducting disks at radii between 10λ and 20λ .

This work was supported by EPSRC-UK under grant No. GR/D034264/1 and the Royal Society through an International Joint Project No. 2005/R1. M.V.M. is a Marie-Curie Intra-European Fellow at the University of Bath. J.R.C. acknowledges support by the Department of Energy - Basic Energy Sciences under Contract No. DE-AC02-07CH11358. T.T. acknowledges support from JSPS bilateral cooperative program.

REFERENCES

- [1] SCHWEIGERT V. A., PEETERS F. M. and SINGHA DEO P., *Phys. Rev. Lett.*, **81** (1998) 2783
- [2] BAELUS B. J., CABRAL L. R. E and PEETERS F. M., *Phys. Rev. B*, **69** (2004) 064506
- [3] KANDA A., BAELUS B. J., PEETERS F. M., KADOWAKI K. and OOTUKA Y., *Phys. Rev. Lett.*, **93** (2004) 257002
- [4] CABRAL L. R. E., BAELUS B. J. and PEETERS F. M., *Phys. Rev. B*, **70** (2004) 144523; see also MISKO V. R., XU, B. and PEETERS F. M., *Phys. Rev. B*, **76** (2007) 024516
- [5] KONG M., PARTOENS B., PEETERS F. M., *Phys. Rev. E*, **67** (2003) 021608
- [6] GRIGORIEVA I. V., ESCOFFIER W., RICHARDSON J., DUBONOS S., VINNIKOV L. Y. and OBOZNOV J., *Phys. Rev. Lett.*, **96** (2006) 077005
- [7] HATA Y., SUZUKI J., KAKEYA I., KADOWAKI K., ODAWARA A., NAGATA A., NAKAYAMA S. and CHINONE K., *Physica C*, **388** (2003) 719
- [8] GEIM A. K., GRIGORIEVA I. V., DUBONOS S. V., LOK J. G. S., MAAN, J. C., FILIPPOV A. E. and PEETERS F. M., *Nature*, **390** (1997) 259

- [9] ZELDOV E., LARKIN A. I., GESHKENBEIN V. B., KONCZYKOWSKI M., MAJER D., KHAYKOVICH B., VINOKUR V. and SHTRIKMAN H., *Phys. Rev. Lett.*, **73** (1994) 1428
- [10] BENKRAOUDA M. and CLEM J. R., *Phys. Rev. B*, **53** (1996) 5716
- [11] ORAL A., BENDING S. J. and HENINI M., *Appl. Phys. Lett.*, **69** (1996) 1324
- [12] BRANDT E. H., *Phys. Rev. B*, **60** (1999) 11939
- [13] BABAEI BROJENY, A. A. and CLEM, J. R., *Phys. Rev. B*, **68** (2003) 174514
- [14] STEPHEN, M. J. and BARDEEN, J., *Phys. Rev.*, **140** (1965) 1197
- [15] PEARL, J., *App. Phys. Lett.*, **5** (1964) 65
- [16] BEDANOV, V. M. AND PEETERS, F. M., *Phys. Rev. B*, **49** (1994) 2667